Slit homogenizer introduced performance gain analysis based on Sentinel-5/UVNS spectrometer

Timon Hummel[1,2], Christian Meister[2], Jasper Krauser[2], and Mark Wenig[1]

[1]Meterological Institute LMU Munich, Theresienstraße 37, Munich, Germany
[2]Airbus Defence and Space GmbH, Willy-Messerschmitt-Str. 1, 82024 Taufkirchen, Germany

Correspondence: Timon Hummel (timon.hummel@airbus.com)

Abstract.

The spectral accuracy of high resolution Earth observation spectrometer missions is affected by the impact of spatially heterogeneous Earth radiance scenes on the instrument spectral response function (ISRF). As the ISRF is the direct link between the forward radiative transfer model and the spectra measured by the instrument, distortions of the ISRF owing to radiometric inhomogeneity of the imaged Earth scene will degrade the precision of the Level-2 retrievals. Therefore, the spectral requirements of an instrument are often parametrized in the knowledge of the ISRF over non-uniform scenes in terms of shape, centroid position of the spectral channel and the Full Width at Half Maximum (FWHM).

The Sentinel-5/UVNS instrument is the first push-broom spectrometer that makes use of a concept referred as slit homogenizer (SH) for the mitigation of spatially non-uniform scenes. This is done by employing a spectrometer slit formed by two parallel mirrors, scrambling the scene in along track direction (ALT) and hence averaging the scene contrast only in the spectral direction. The flat mirrors do not affect imaging in the across track direction (ACT) and thus preserve the spatial information in that direction. The multiple reflections inside the SH act as coherent virtual light sources and the resulting interference pattern at the SH exit plane can be described by simulations using scalar diffraction theory.

By homogenizing the slit illumination, the SH moreover strongly modifies the spectrograph pupil as a function of the input scene. In this work we investigate the impact and strength of spectrograph pupil variations for different scene cases and quantify the impact on the ISRF stability for different type of aberrations present in the spectrograph optics.

1 Introduction

The Ozone Monitoring Instrument (OMI) was the first instrument identifying the issue arising from non-uniform Earth scenes on the shape and maximum position of the spectral response of the instrument (Voors et al., 2006). As in most space based imaging spectrometer, the Earth radiance scene gets imaged by the telescope onto the instrument entrance slit plane. In the subsequent spectrograph, the slit illumination gets spectrally resolved by a dispersive element and eventually re-imaged on the focal plane array (FPA) by an imaging system. During the imaging process, the slit illumination intensity distribution gets convoluted by the spectrograph point spread function (PSF) and the detector pixel characteristics. The resulting intensity pattern on the FPA in the spectral direction is called the instrument spectral response function (ISRF). Depending on the observed scene

25   heterogeneity, the entrance slit will be inhomogeneously illuminated and will alter the ISRF (see Fig. 1). Moreover, a scene dependency in the PSF will also affect the ISRF, which will be particularly discussed in this manuscript. As the ISRF is the direct link between the radiative transfer model and the spectrum measured by the instrument, a scene dependent shape of the ISRF will have an immediate impact on the accuracy of the Level2-retrieval products. Figure 2 depicts a representative Top-of-Atmosphere spectrum in the SWIR wavelength band, entering a space-borne instrument. The high-resolution spectrum will

30   be smeared by means of a convolution with an exemplary ISRF, which depends on the imaging properties of the instrument for every monochromatic stimulus. Whenever the ISRF shape deviates from the on-ground characterized shape, due to for example heterogeneous scenes, it will affect the measured spectrum, which serves as a basis for the applied retrieval algorithms.
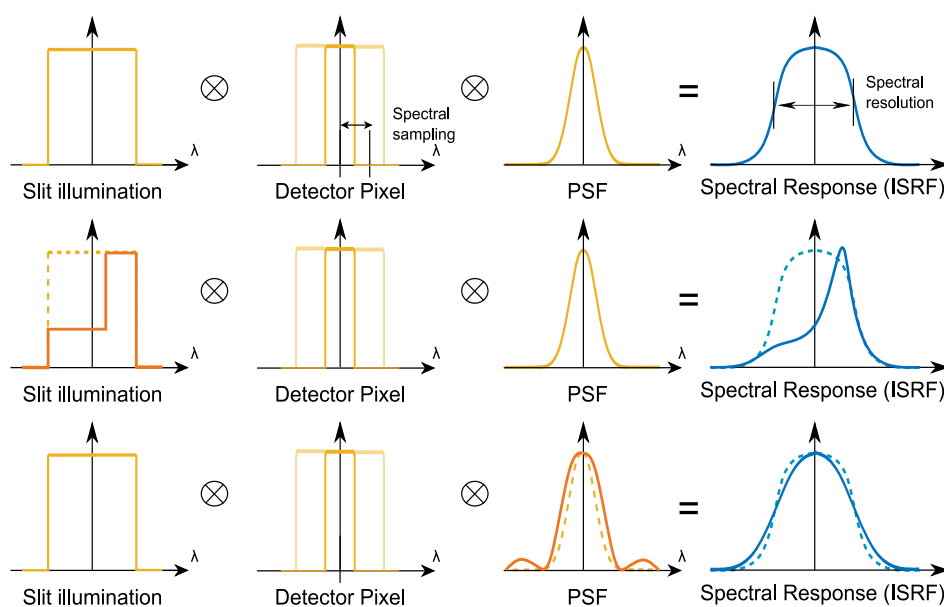
Figure 1. The ISRF of an imaging spectrometer is given by the convolution of the slit illumination, pixel response and the optical PSF of the spectrograph optics. In the context of heterogeneous scenes, the ISRF can be altered due to non-uniform illumination and instabilities in the optical PSF. This leads to deformation in the ISRF with respect to the centroid, shape and the FWHM.

     This effect is particularly prominent for instruments with a high spatial resolution. The along track motion of the satellite accounting for the spectral direction of the spectrometer serves as an averaging and smearing effect of the scene. Spectrometers

35   with a large scan area like GOME (Burrows et al., 1999) or SCHIAMACHY (Bovensmann et al. (1999), Burrows et al. (1995)) are less vulnerable to contrast in the Earth scene. In contrary, recent high resolution hyperspectral imaging spectrometer define a set of stringent requirements on the inflight knowledge and stability of the ISRF. This is necessary, as distortions in the ISRF due to non-uniform scenes will introduce biases in the Level-2 data and therefore in the precision of atmospheric composition products. For the 2017 launched Sentinel-5 Precursor (S5P) satellite with the Tropospheric Monitoring Instrument (TROPOMI)

40   being the single payload, Hu et al. (2016) showed that the stability and knowledge of the ISRF is the main driver of all
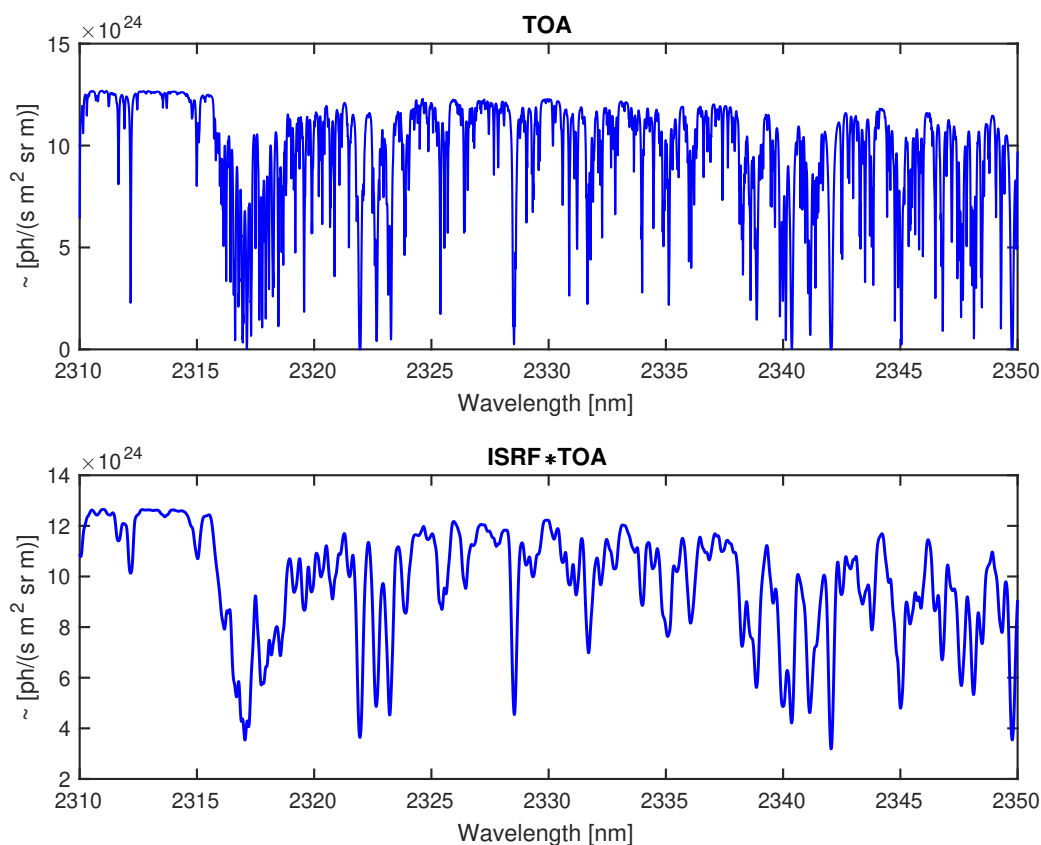
Figure 2. (Top) Representative high-resolution Earth Top-of-Atmosphere (TOA) spectrum entering a space-borne instrument in the SWIR-3 wavelength band. (Bottom) TOA spectrum convolved with a constant exemplary ISRF. Whenever the ISRF deviates from the the on-ground characterized shape, the measured spectrum, which sets the basis for the retrieval algorithms, will be altered.

instrument calibration errors for the retrieval accuracy. Landgraf et al. (2016) estimate the error of the retrieved CO data product due to non-uniform slit illumination to be in the order of 2% with a quasi random characteristics. Noël et al. (2012) quantify the retrieval error for the Sentinel-4 UVN imaging spectrometer for the tropospheric O_3, NO_2, SO_2 and HCHO. They identify a difference in the retrieval error depending on the trace gas under observation. The largest error occurs for NO_2

45   with a mean error of 5% and a maximum error of 50%. They propose a software correction algorithm which is based on a wavelength calibration scheme individually to all Earthshine radiance spectra. As discussed by Caron et al. (2019), this type of software correction can only be applied to dedicated bands (UVN, UV-VIS) but is failing particularly in the SWIR absorption band due to the strong absorption bands of highly variable atmospheric components.

Sentinel-5/UVNS (Irizar et al., 2019) is the first push-broom spectrometer that employs an onboard concept to mitigate the

50   effect of non-uniform scenes. A hardware solution called slit homogenizer (SH) is implemented which reduces the scene contrast of the Earth radiance by replacing the classical slit with a pair of two parallel extended mirrors in the along track

direction (ALT) of the satellite flight motion (Fig. 3a). The distance between the two parallel rectangular mirrors is of $b = 240\,\mu m$ (NIR), side lengths of $65\,mm$ in ACT and a length of $9.6\,mm$ along the optical axis. Thereby, the light focussed by the telescope optics onto the slit entrance plane gets scrambled in the ALT direction, whereas the light in ACT passes the

55   SH without any reflection. For a realistic reference Earth scene of the Sentinel-5/UVNS mission provided by ESA (S5-ESA-scene), the total in orbit ISRF shape error budget is $< 2\,\%$, the relative Full width half Maximum (FWHM) error $< 1\,\%$ and the centroid error in the NIR $0.02\,nm$. Meister et al. (2017) and Caron et al. (2019) presented simulation results providing a first order performance validation prediction of the SH principle, which are relevant to achieve the performance requirements above. However, so far several second order effects haven't been quantitatively addressed in the homogenization performance

60   prediction. This paper extents the existing first-order models and provides a more elaborated and comprehensive description of the SH and its impact on performance and instrument layout. We present an end-to-end model of the Sentinel-5/UVNS NIR channel ($760\,nm$). In particular, we determine the spectrograph pupil illumination which is altered by the multiple reflections inside the SH. This effect changes the weighting of the aberrations present in the spectrograph optics and consequently implies a scene dependency in the optical PSF. As the ISRF is not only a function of the slit illumination, but also of the spectrograph

65   PSF, a variation in the spectrograph pupil intensity distribution will ultimately put an uncertainty and error contribution to the ISRF. The severity of the spectrograph illumination distortion highly depends on the slit input illumination and the strength and type of aberrations present in the spectrograph. In order to quantify the achievable ISRF stability, we simulate several input scenes and different type of aberrations.

The outline of this paper is as follows: Sect. 2 describes the model we deployed to propagate the light through the SH by

70   Huygens-Fresnel-diffraction formula. Applying Fourier optics, we formulate the propagation of the complex electric field from the SH exit plane up to the grating position, representing the reference plane for the evaluation of the spectrograph pupil intensity distribution. In Section 3 we quantify the spectrograph pupil intensity distribution for several Earth scene cases. The scene dependent weighting of the aberrations in the spectrograph and its impact on the ISRF properties is discussed and quantified in Sect. 4. Finally, we summarize our results in Sect. 5.

2   Slit Homogenizer Model

This section contains details on the underlying models and the working principle of the SH. The first part briefly summarizes the model developed by Meister et al. (2017), which describes the field propagation through the Sentinel-5/UVNS instrument up to the SH exit plane by using a scalar-diffraction approach. The second part focusses on the novel modelling technique of the spectrograph optics. We put a particular focus on the scene dependency of the spectrograph illumination while using a SH.

2.1   Near Field

The light from objects on the Earth that are imaged at one spatial position (along slit) within the homogenizer entrance slit arrive at the Sentinel-5/UVNS telescope entrance pupil as plane waves, where the incidence angle θ is between $\pm 0.1°$. The extent of the wavefront is limited by the size and shape of the telescope aperture. Neglecting geometrical optical aberrations,

the telescope would create a diffraction limited point spread function with the characteristic airy disc size in the telescope

85 image where the SH entrance slit is positioned. Depending on the angle of incidence, the PSF centroid will be located at a dedicated position within the entrance slit. The characteristic airy disc in the entrance slit plane is given as (Goodman, 2005, p. 103)

$$\tilde{U}_{f,\theta}(u,v) = \frac{A}{i\lambda f} e^{-i\frac{k}{2f}\left(u^2+v^2\right)} \int_{\Omega} e^{iky\,sin(\theta)} e^{-i\frac{k}{f}(xu+yv)}\,dxdy \tag{1}$$

$$= \frac{iAD^2}{\lambda f} e^{-i\frac{k}{2f}\left(u^2+v^2\right)} sinc\left(\frac{Dk}{2f}u\right)\,sinc\left(\frac{Dk}{2f}(fsin(\theta))\right) \tag{2}$$

90 where (x,y) are the coordinate positions in the telescope entrance pupil and (u,v) are the respective coordinates in the SH entrance plane. Ω denotes the two-dimensional entrance pupil area, f is the focal length of the telescope, A the amplitude of the plane wavefront at the telescope entrance pupil, D the full side length of the quadratic telescope entrance pupil and $k = \frac{2\pi}{\lambda}$ the wavenumber. Further, the relation $\int_{-a}^{a} e^{ixc} = 2asinc(ca)$ and a Fresnel approximation was applied in Eq. (2). The propagation of $\tilde{U}_f$ through the subsequent SH is described by the Huygens-Fresnel principle (Goodman, 2005, p. 66). The reflections at the

95 two mirrors are accounted for by inverting the propagation component in ALT upon every reflection n as

$$U_{f,\theta}(u,v) = R^{|n|} e^{in\pi} \tilde{U}_{f,\theta}\left(u,(-1)^n(v-nb)\right), \qquad \text{for } v \in \left[-\frac{b}{2}+nb, \frac{b}{2}+nb\right] \tag{3}$$

where R is the reflectivity and $e^{in\pi}$ describes a phase jump upon every reflection n. Inserting Eq. (2) into (3) and applying the Huygens-Fresnel diffraction principle yields the expression for the intensity distribution at the SH exit plane for a given incidence angle θ, SH length l and position $r(u,v) = \sqrt{l^2+(x-u)^2+(y-v)^2}$ as

$$U_\theta(x,y) = \frac{lAD^2}{\lambda^2 f} \int_{u\in\mathbb{R}} \int_{v=-\frac{b}{2}}^{v=\frac{b}{2}} \sum_{n\in\mathbb{N}} R^{|n|} \frac{e^{i\frac{k}{2f}\left(u^2+((-1)^n(v-nb))^2\right)+ikr(u,v)+in\pi}}{r^2(u,v)}$$

100

$$\cdot sinc\left(\frac{Dk}{2f}u\right) sinc\left(\frac{Dk}{2f}(fsin(\theta)-(-1)^n)\right) \tag{4}$$

Evaluating Eq. (4) for every incidence angle of the Sentinel-5/UVNS field of view results in the so called SH transfer function (Fig. 3b), which maps any field point originating from Earth to an intensity distribution at the SH exit plane. In a purely geometric theory and a perfect SH configuration in terms of length, every point source would be distributed homogeneously in ALT direction (Fig. 3a). However, as is quantified in Eq. (4), the field distribution at the SH output plane highly depends on

105 interference effects due to path differences of the reflected light inside the SH, resulting in a non-uniform transfer function as shown in Fig. 3a.

(a) Slit homogenization

(b) SH transfer function
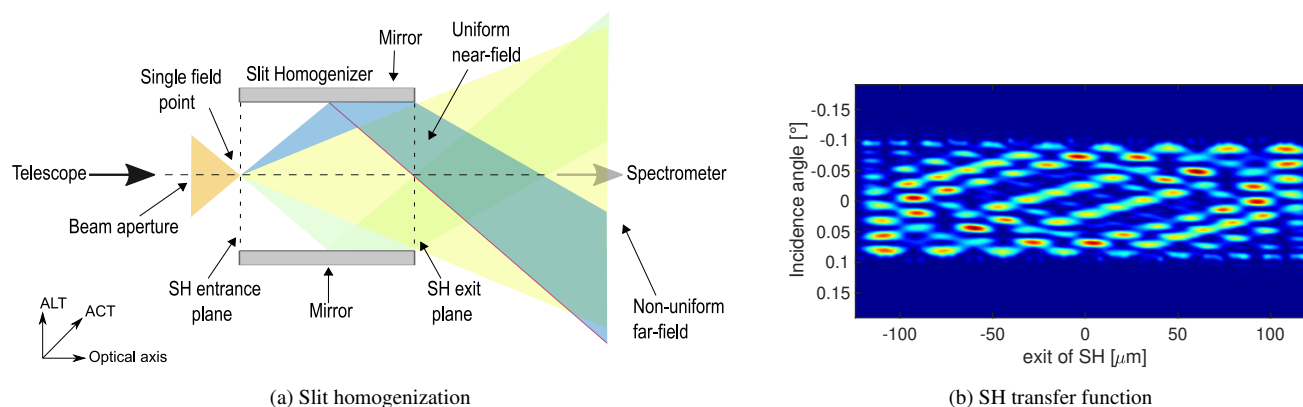
Figure 3. (a) The SH homogenization principle based on a purely geometrical concept. With an appropriate length selection, the SH would perfectly homogenize any input scene. (b) SH transfer function. In reality, the output pattern of the SH is highly dependent on interference effects.

2.2 Far Field

In a space-based imaging spectrometer equipped with a classical slit acting as a field stop, a point source on the Earth surface enters the instrument as a plane wavefront with a uniform intensity over the telescope pupil. As this principle applies for every point source in a spatial sample on the Earth, the telescope pupil intensity homogeneity is independent of the radiance variation among the point sources in a spatial sample. Besides some diffraction edge effects in the slit plane, the telescope pupil intensity distribution gets retrieved in the spectrograph pupil. This is not the case when introducing a mirror based SH. Existing SH models (Meister et al. (2017) and Caron et al. (2019)) implement the spectrometer as a simple scaling factor and the ISRF on the FPA is obtained via the convolution of the SH output intensity distribution, the pixel response implemented as a characteristic function and the spectrograph PSF. In this contribution we model the propagation through the spectrograph more accurately by including the spectrograph optics, such as the collimator, a dispersive element and the imaging optics. In particular, the inclusion of these optical parts becomes important because the SH not only homogenizes the scene contrast in the slit, but it also significantly modifies the spectrograph pupil. A schematic diagram of the SH behaviour and the instrument setup is shown in Fig. 4. A plane wavefront with incidence angle Θ is focussed by a telescope on the SH entrance pupil. In ACT direction, the light is not affected by the SH. After a distance l, corresponding to the SH length, the diffraction limited PSF at the SH entrance pupil is converted to the far field pattern of the diffraction limited airy-disc. Independent of the applied scene in ACT, the telescope pupil is retrieved again at the spectrograph pupil despite a magnification factor and a truncation of the electric field at the SH entrance plane, which leads to a slight broadening and small intensity variations with a high frequency in angular space (Berlich and Harnisch, 2017). In ALT the light airy-disc pattern in the SH entrance plane undergoes multiple reflections on the mirrors, so that eventually the whole exit plane of the SH is illuminated. Hence, the object plane is defocused by the SH length. Moreover, the multiple reflections inside the SH lead to a modification of the system exit pupil. In other words, the SH output plane (near field) and the spectrograph pupil intensity variation (SH far field) strongly depend on the
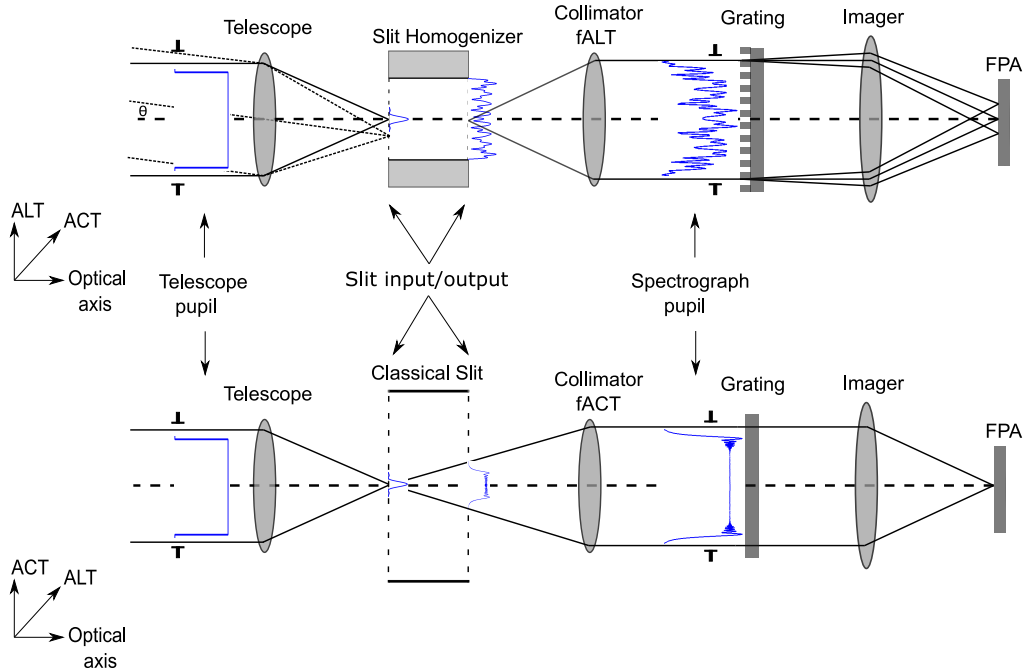
Figure 4. Generic setup of the SH in the Sentinel-5/UVNS instrument. A plane wavefront gets focussed in the SH entrance plane and the propagation of such stimulus is shown in blue as the square modulus of the electric field. The incoming light undergoes several reflections in ALT direction, whereas the SH in ACT is similar to a classical slit acting as a field stop. The slit homogenizes the scene in ALT direction but also modifies the spectrograph pupil. The grating is a 1D binary phase grating which disperses the light in ALT. The pupil distribution in ACT direction is conserved except for diffraction effects due to truncation of the telescope PSF in the slit plane.

initial position of the incoming plane wave, and therefore on the Earth scene radiance in ALT direction. Following a first simple geometrical argument as discussed by (Caron et al., 2019), we consider a point source at the SH entrance. The rays inside

130   the cone emerging from this source will undergo a number of reflections depending on the position of the point source and the angle of the specific ray inside the cone. The maximum angle is given by the telescope F-Number. With this geometrical reasoning it becomes obvious, that the number of reflections differs among the rays inside the cone. If the number of reflections is even, a ray keeps its nominal pupil position; whereas if the number is odd, its pupil coordinate will be inverted. From this argument we deduce that the spectrograph pupil will be altered with respect to the telescope pupil. In the following we make

135   this argument rigorous using diffraction theory. A general case for the connection between slit exit plane and spectrograph pupil plane is considered by Goodman (2005, p. 104). In the scenario discussed there, a collimated input field $U_l(x,y)$ propagates through a perfect thin lens at a distance d. The field in the focal plane of the lens is then given by:

$$U_f(u,v) = \frac{A}{i\lambda f} \, exp\left(i\frac{k}{2f}\left(1-\frac{d}{f}\right)(u^2+v^2)\right) \int\limits_{-\infty}^{\infty}\int\limits_{-\infty}^{\infty} U_l(x,y) \, exp\left(-i\frac{2\pi}{\lambda f}(xu+yu)\right)dxdy \qquad (5)$$

where k is the wavevector of the incoming wave, λ is the wavelength and f is the focal length of the lens. Hence, the field at
140   the lens focal plane is proportional to the two-dimensional Fourier transform.

     In contrast, our situation is inverted as we are interested in $U_l(x, y)$, i.e. the collimated field distribution after the collimation
optics originating from the SH output plane. By using Fourier theory and applying $d = f_{col,ALT}$ we obtain the field distribution
at the position of the diffracting grating as:

$$U_l\left(\frac{2\pi}{\lambda f}\, x, \frac{2\pi}{\lambda f}\, y\right) = \frac{i}{A\lambda f} \int \int\limits_{-\infty}^{\infty} \int\limits_{-\infty}^{\infty} U_f(u,v)(u^2+v^2)\, exp\left(-i\frac{2\pi}{\lambda f}(xu+yv)\right) du\, dv \tag{6}$$

145

2.3   Collimator astigmatism

The multiple reflections inside the SH in the ALT-dimension induces an anamorphism which means, that we get different
object planes in ALT and ACT direction. The separation between the focal points corresponds exactly to the length of the SH.
150   This is compensated by an astigmatism introduced on the collimation optics. In our model, this is implemented via Zernike
polynomial terms on the collimation lens. We follow the OSA/ANSI convention for the definitions of the Zernike polynomials
and the indexing of the Zernike modes (Thibos et al., 2000). For the focal length of the collimation optics we match the object
plane in ALT direction, which corresponds to the SH exit plane. The first contribution to the Zernike term is a defocus with an
appropriate coefficient, which shifts the object position from the SH exit plane to the centre of the SH. From there, we apply
155   an astigmatism, which splits up the object plane into a sagittal focus corresponding to the telescope focus in ACT (SH input
plane) and a tangential focus corresponding to the focus position in ALT (SH exit plane). The Zernike polynomials are given
by:

$$\text{Defocus:} \quad Z_n^m(\rho,\theta) = Z_2^0(\rho,\theta) = c\sqrt{3}(2\rho^2 - 1) \tag{7}$$

$$\text{Astigmatism:} \quad Z_n^m(\rho,\theta) = Z_2^2(\rho,\theta) = c\sqrt{6}\rho^2 sin(2\theta) \tag{8}$$

160   where c is the Zernike coefficients, defining the strength of the aberration and Z_n^m the Zernike polynomials. Due to the elegant
and orthonormal definition of the Zernike polynomials, a perfect matching of Defocus and Astigmatism amplitude is straight
forward, as the difference between the sagitta and tangential plane of the astigmatism is solely dependent on the radial term of
the Zernike polynomial. Therefore, in order to match the corresponding difference given by the SH length, the weighting of
the astigmatism has to be larger than the defocus term by a factor of $\sqrt{2}$, which can be derived by comparing the prefactor of
165   the radial terms in Z_n^m of Defocus and Astigmatism. Hence, the combined Zernike term will be:

$$H(\rho,\theta) = c\, Z_2^0(\rho,\theta) + \sqrt{2}\, c\, Z_2^2(\rho,\theta) \tag{9}$$

Including the astigmatic correction of the collimation optics in the wavefront propagation modifies equation 6 into:

$$U_l\left(\frac{2\pi}{\lambda f}\,x, \frac{2\pi}{\lambda f}\,y\right) = \frac{i}{A\lambda f} e^{-\frac{ik}{\pi}\left(c\,Z_2^0(\rho,\theta) + \sqrt{2}\,c\,Z_2^2(\rho,\theta)\right)}$$
$$\cdot \int_{-\infty}^{\infty}\int_{-\infty}^{\infty} U_f(u,v)(u^2+v^2)\ exp\left(-i\frac{2\pi}{\lambda f}(xu+yv)\right) dudv \tag{10}$$

170

2.4 Diffraction grating

The primary goal of the spectrometer is to distinguish the intensity of the light as a function of the wavelength and spatial position. In order to separate the wavelengths a diffractive element is placed in the spectrograph pupil and disperses the light in the ALT direction. For our analysis, we place the diffraction grating at a distance $d = f_{col,ALT}$ after the collimator and on the

175 optical axes. Further, we model the dispersive element as a 1D binary phase diffraction grating. Such gratings induce a π phase variation by thickness changes of the grating medium. Three design parameters are used to describe the grating and are unique for every spectrometer channel: the period of the grating Λ, the phase difference Φ between the ridge (of width d), the groove regions of the grating and the fill factor d/Λ. Physically, the phase difference itself is induced by two parameters: the height or thickness t of the ridge and the refractive index of the material of which the grating is made. In most cases, the refractive index

180 of the used material is fixed and the thickness of the material is the primary parameter. The phase profile with a fill factor of 0.5 which provides the maximum efficiency in ALT direction is given by:

$$\Phi_{1D}(y) = \begin{cases} \pi & 0 \leq y \leq \frac{\Lambda}{2} \\ 0 & \frac{\Lambda}{2} \leq y \leq \Lambda \end{cases} \tag{11}$$

The complex electric field of the spectrograph pupil wavefront after the diffraction grating is then given by:

$$U_g(x,y) = U_l(x,y)\,e^{i\Phi(y)} \tag{12}$$

185 The intensity distribution after the grating is given by inserting equation (10) in (12) and applying the absolute square:

$$I_g(x,y) = |U_g(x,y)|.^2 \tag{13}$$

3 Spectrograph pupil intensity distribution

The far field intensity distribution is highly dependent on the contrast of the Earth scene in ALT and therefore on the SH entrance illumination. In order to characterize the amplitude of the spectrograph pupil intensity distribution, we introduce

190 several Earth scene cases and therefore slit illuminations in ALT as depicted in Fig 5. The test cases contain a uniform scene, a representative Earth scene for the Sentinel-5/UVNS instrument provided by ESA (S5-ESA-scene) and stationary high contrast

calibration scenes, which corresponds to the case where the SH ALT entrance plane is partially illuminated by 75 %, 50 % and 25 %. Further, we also show the spectrograph pupil for a single point source at the SH entrance. Fig. 5 shows the top of atmosphere (ToA) radiance level given by a realistic Earth scene for the Sentinel-5/UVNS instrument. Due to smearing of the

195   satellite's movement, this scene has a significantly lower contrast than the calibration scenes. Here we want to emphasize that future missions depending on their spatial and spectral resolution as well as their desired data product may have even more stringent requirements on the scene homogeneity. The CO_2 Monitoring Mission (CO2M) aims to detect strong, almost point like CO_2 and CH_4 emission sources with a spatial resolution of 4 km^2 (Sierk et al., 2019). In order to achieve a maximum error of XCO_2 of 0.5 ppm, an ISRF shape stability of < 1.5 % over a maximum contrast scene is required. This corresponds

200   to a sharp transition from bright to dark slit illumination as shown for the calibration scenes in Fig. 5.
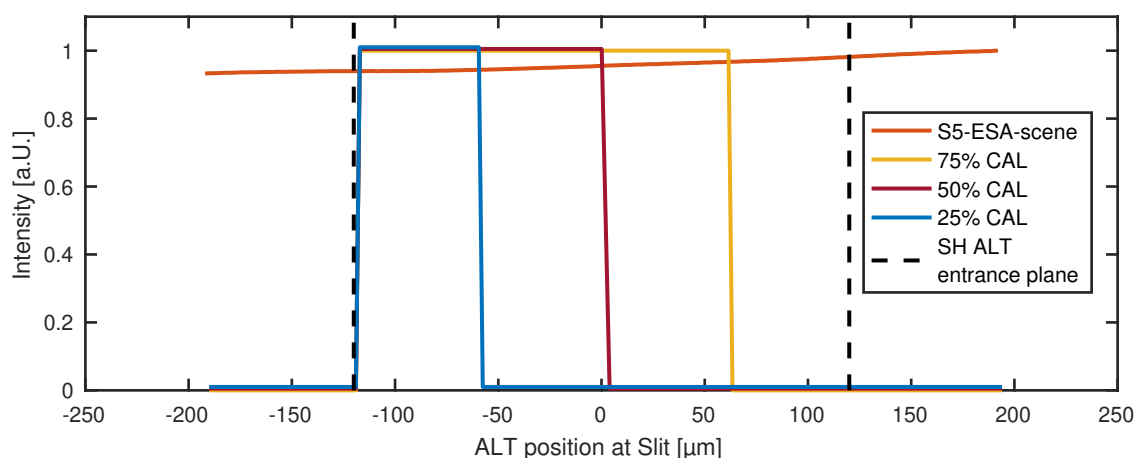
Figure 5. Applied input Earth scenes corresponding to the slit illumination in ALT. This includes a representative scene for the Sentinel-5/UVNS instrument and several high contrast calibration scenes with 75%, 50% and 25% slit illumination.

   Figure 6 depicts the pupil intensity distribution in the NIR (760 nm) for the applied test scenes. As expected, the uniformity of the input telescope pupil is completely conserved in ACT direction as no interaction, i.e. reflection, with the SH is happening. Therefore the top-hat intensity distribution of the telescope is, besides diffraction edge effects, completely retrieved. Contrary, the intensity distribution in ALT is highly dependent on the contrast of the applied scene. Even for a homogeneous scene the

205   SH modifies the pupil intensity (Fig. 6a) and consists of symmetrical variations. The intensity pattern just varies slightly for the S5-ESA-Scene (Fig. 6b) due to the low contrast in the scene. However, for high contrast calibration scenes (Fig. 6 c,d,e) the SH drastically disturbs the uniformity of the spectrograph pupil, leading to a maximum of 80 % peak to valley intensity modulation (e).

(a) Homogeneous scene

(b) S5-ESA-scene

(c) 75 % along slit illumination

(d) 50 % along slit illumination

(e) 25 % along slit illumination

(f) Single point source at SH entrance plane
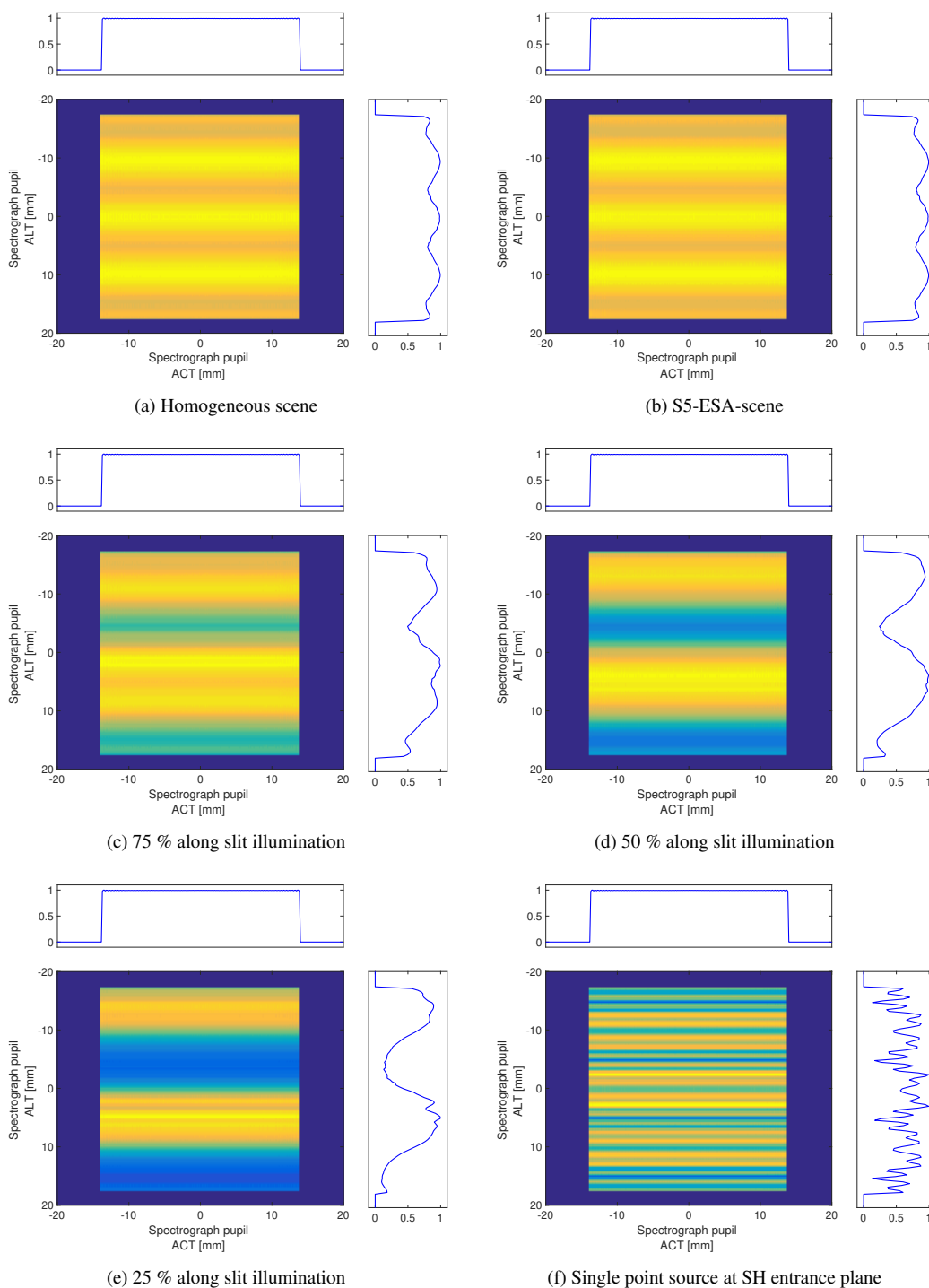
Figure 6. Spectrograph pupil intensity distribution in the NIR (760 nm) for different slit illuminations. The uniformity of the pupil in ALT is highly dependent on the applied scene. As expected the ACT uniformity from the telescope pupil is conserved as there is no interaction with the SH.

4 Impact on ISRF

210 The main impact of the above described variations in the spectrometer pupil illumination is the scene dependent weighting of the aberrations inherent to the spectrograph optics. In a simplified view, the ISRF of an imaging spectrometer is given by the convolution of the slit illumination, the pixel response on the FPA and the optical PSF of the spectrograph optics. A scene dependency of the spectrograph pupil illumination will weight the aberrations of the system accordingly and thereby create an error in the PSF, which will ultimately also affect the ISRF properties.

215   Instead of convolution, we propagate the spectrograph pupil through the imaging optics by diffraction integrals. For the description of the aberrations present in the Sentinel-5/UVNS instrument we use again the formulation of Zernike theory. We know from ray tracing simulation predictions the PSF size on the FPA of the Sentinel-5/UVNS NIR channel, which in a simplified model is given by the standard deviation of a normal distribution. As the actual aberrations present in the system are yet unknown, we impinge different types of aberrations on the spectrograph imaging optics and match the PSF size to the

220 design prediction. As the shape of the PSF for an arbitrary aberration is not given by a normal distribution, we define the PSF size as the area where $80\,\%$ of the encircled energy (EE) is contained. Then we tune the strength of the aberration coefficients in such a way that the size of the aberrated PSF matches the case where we assume a normal distribution as PSF. For the transformation of the spectrograph pupil to the FPA including aberrations, we apply the thin lens formula and expand it by adding the phase term for the Zernike aberrations (Goodman, 2005, p. 145). Our starting point for the propagation is the grating

225 position where, for the case of Sentinel-5/UVNS, the distance d is matching the focal length of the imaging optics. In that case the formulation simplifies again and is given by a relation which has the form of a Fourier transform:

$$U_{FPA}(u,v) = \frac{2\pi}{i\lambda f_{im}} \int_{-\infty}^{\infty} \int_{-\infty}^{\infty} U_g(x,y)\, exp\left(-i\frac{2\pi}{\lambda f_{im}}(xu+yu)\right)\, exp\left(\frac{-ik}{\pi}\, H(r,\phi)\right) dxdy \qquad (14)$$

where f_{im} is the focal length of the imager, U_g the field distribution at the grating and $H(r,\phi)$, with $r = r(x,y)$ and $\phi = \phi(x,y)$, the respective Zernike aberration that we apply. Any spatially incoherent monochromatic input scene can be distributed

230 in plane wavefronts with amplitude $A(\Theta)$. Each such wavefront leads to an intensity $I = I_\Theta(u,v) = |U_{FPA}|^2$ on the FPA. As we have no SH impact in ACT direction, we collapse this dimension and sum along it. This yields the $1D$ ISRF intensity distribution on the FPA as a function of the incidence angle Θ as $I_\Theta(v)$. The respective scene will weight the intensities on the FPA depending of their strength and is therefore the linear operator:

$$I_v = \int_{\Theta \in \mathcal{R}} A(\Theta)I(\Theta,v)\, d\Theta = I \circ A(v) \qquad (15)$$

235 Note that for a homogeneous scene, $A(\Theta) = 1$ for every incidence angle. Finally, the normalized ISRF on the FPA is given by:

$$\widetilde{ISRF}(v) = ((I_\Theta \circ A)\, *\chi * N_\sigma(v) \qquad (16)$$

$$ISRF(v) = \frac{\widetilde{ISRF}(v)}{\alpha \int \widetilde{ISRF}(v)dv} \qquad (17)$$

where χ is the characteristic function, which is 1 inside a pixel area and 0 elsewhere, α a scaling factor to give the ISRF in units of wavelength and N_σ is the density function of a normal distribution with zero mean value and standard deviation σ. The latter factor accounts for the modulation transfer function (MTF) of the detector (not the MTF of the whole optical system). In order to asses the stability of the ISRF we define three merit functions:

- Shape error, which we define as the maximum difference of the ISRF calculated for a homogeneous and heterogeneous scene respectively

$$\text{Shape error} := \max_{v}\left|\frac{ISRF_{hom}(v) - ISRF_{het}(v)}{\max_{\tilde{v}} ISRF_{hom}(\tilde{v})}\right| \tag{18}$$

- Centroid error: Shift of the position of the spectral channel centroid, where the centroid is defined as

$$\text{Centroid} := \frac{\int\limits_{FPA} ISRF(v)\ v\ dv}{\int\limits_{FPA} ISRF(v)} \tag{19}$$

- Spot size of the ISRF given by the FWHM

For our assessment of the induced change in ISRF stability, we distinguish three different cases of calculation. First, we calculate the ISRF merit functions (Shape, centroid, FWHM) for the case, where the PSF is given by a normal distribution simply defined as:

$$g(v) = \frac{1}{\sigma\sqrt{2\pi}}\ exp\left(-\frac{v^2}{2\sigma^2}\right) \tag{20}$$

where σ is the standard deviation representing the size of the PSF (e.g. 19.1 μm in NIR [1] for a representative field point). In that case, we neglect the non uniformity in the pupil and the spectrometer aberrations. For the second case, we impinge a certain amount of pure spherical aberrations on the imaging optics to get the same spot size for the PSF as in case 1. Spherical aberrations are radially symmetric like the Airy pattern itself and the size of the central bright spot does not change with increasing amount of spherical aberrations. As a third case, we apply pure comatic aberrations, which behave fundamentally different than spherical aberrations and have radial and azimuthal contributions in the phase map. The wavefront errors induced by comatic aberrations have reverse symmetry along the axis of aberration, with one side flatter and the other more curved with respect to its perfect reference wavefront. Their formulation in Zernike polynomials is given by:

$$\text{Spherical Aberration}: \quad Z_n^m(\rho,\theta) = Z_4^0(\rho,\theta) = c\sqrt{5}(6\rho^4 - 6\rho^2 + 1) \tag{21}$$

$$\text{Vertical Coma}: \quad Z_n^m(\rho,\theta) = Z_3^{-1}(\rho,\theta) = c\sqrt{8}(\rho^3 - 2\rho)sin(\theta) \tag{22}$$

Clearly, a scene dependent mixture of the aberration weighting will create different result for the properties of the subsequently calculated ISRF. As the spectrograph pupil homogeneity, similar to the SH exit plane, is highly dependent on the

---

[1]Preliminary analytical value

scene that we apply, we calculate the ISRF properties for the scenes defined in Fig. 5. As a direct comparison of the difference
between an ISRF calculated with a PSF disturbed by aberrations and a PSF given as a pure normal distribution is problematic,
we rather compare the errors relative to a homogeneous scene.

Table (1-3) summarizes the result of our calculations. It shows the errors for the ISRF merit functions, where the PSF is cal-
culated with a normal distribution (1), pure spherical aberrations (2) and comatic aberrations (3) for different SH input scenes.
As expected, the absolute error goes up for every case as we apply higher scene contrasts. In first order, this comes from the
lacking capability of the SH to reduce very high scene contrasts and thereby the slit imaged on the detector has still prominent
remnants of the scene contrast at the SH entrance plane. However as a secondary effect, we see that the strength of the errors
is also critically dependent on the PSF specified by the aberrations that we apply and their respective weighting by the pupil
intensity distribution. As expected, radially symmetric aberrations have no impact on the centroid and shape error but induce
a higher FWHM error. Even for a scene with limited contrast as the S5-ESA-scene the FWHM error goes up by an order of
magnitude. On the other hand, comatic aberrations degrade the ISRF stability in terms of shape error and FWHM error. For the
S5-ESA-scene, the shape error more than doubles and the FWHM error goes up by a factor of 8. For the calibration scenes, the
error contribution gets significantly higher due to higher non uniformity in the spectrograph pupil. As the slit illumination and
therefore mixing of the scene contrast in the SH exit plane is the same for all three PSF cases, it seems a valid assumption, that
the difference in the relative errors comes only by the non uniform intensity in the spectrograph pupil. As the discrepancy in the
values is quite significant, we believe that depending on the mission parameters, this effect should be taken into account for the
assessment of the ISRF stability and consequently the performance of the SH. We also conclude, that for the Sentinel-5/UVNS
instrument the impact of this effect is of second-order and doesn't degrade the performance of the SH significantly.

Table 1. PSF given as normal distribution $EE_{80\,\%} = 19.1\,\mu m$ (NIR)

Scene	ISRF shape error [%]	ISRF centroid error [nm]	ISRF FWHM error [%]
S5-ESA-Scene	0.088	-1.444E-04	0.001
75 % CAL Scene	2.963	4.795E-03	0.340
50 % CAL Scene	5.864	9.639E-03	0.742
25 % CAL Scene	9.097	1.472E-02	3.060

Table 2. PSF with pure spherical aberrations $EE_{80\,\%} = 19.1\,\mu m$ (NIR)

Scene	ISRF shape error [%]	ISRF centroid error [nm]	ISRF FWHM error [%]
S5-ESA-Scene	0.061	8.406E-05	0.011
75 % CAL Scene	2.421	2.899E-03	1.220
50 % CAL Scene	3.802	5.500E-03	0.038
25 % CAL Scene	7.080	8.739E-03	3.601

Table 3. PSF with pure comatic aberrations $EE_{80\,\%} = 19.1\,\mu m$ (NIR)

Scene	ISRF shape error [%]	ISRF centroid error [nm]	ISRF FWHM error [%]
S5-ESA-Scene	0.184	1.436E-04	0.082
75 % CAL Scene	5.694	4.471E-03	2.394
50 % CAL Scene	12.184	9.530E-03	1.047
25 % CAL Scene	21.387	1.528E-02	7.106

5 Conclusion

285 In this paper we presented an end-to-end simulation of the Sentinel-5/UVNS Slit-homogenizer and demonstrated the impact of non-uniform scenes on the spectrograph pupil intensity distribution. A scene dependency of the spectrograph pupil will lead to similar ISRF distortion as due to non-uniform slit illuminations resulting in a pseudo-noise contribution in the measured ToA reflectance. This error source of the final data product will affect the accuracy of the trace gas derivation of the reflectance spectra. The severity of the error is crucially dependent on contrast, which the instrument will see during a single integration

290 time. A representative scene of the Sentinel-5/UVNS instrument has a rather weak contrast and therefore the instrument fulfils the ISRF specifications in order to meet the Level-2 performance requirements of the mission. In contrast to this, future missions like CO2M have to be compliant with higher contrast scenes with almost a sharp transition from dark to bright slit illuminations. In such cases, the spectrometer illumination will vary drastically and puts another uncertainty to the ISRF due to PSF variations. We confirmed that Sentinel-5/UVNS meets the requirements on the ISRF knowledge including the modified

295 intensity distribution in the spectrograph pupil and accounting for optical aberrations present in the spectrometer optics. The contribution of the residual errors due to representative inhomogeneous ToA scenes are well below the system requirements, which are: shape error $< 2\,\%$, the relative FWHM error $< 1\,\%$ and the centroid error < 0.02 nm (NIR). The application of

the slit homogenizer for missions with high contrast scenes (CO2M) will impose strong variations in the spectrograph pupil and will result in large errors in the ISRF and hence significantly degrades the accuracy in the retrieval of the atmospheric

300   composition and therefore the mission product.

Data availability.   The datasets generated and/or analyzed for this work are available from the corresponding author on reasonable request, subject to confirmation of Airbus Defence and Space GmbH.

Author contributions.   Timon Hummel was responsible for the modelling and the analysis of the simulation data supported by all co-authors. Timon Hummel developed the end-to-end model and the approach to quantify the impact on the ISRF supported and revised by Christian

305   Meister. Timon Hummel prepared the manuscript with contributions and critical revision from all co-authors.

Competing interests.   The authors declare, that they have no conflict of interest.

Acknowledgements.   We thank Tobias Lamour, Jess Köhler and Markus Melf (all Airbus Defence and Space) for the helpful comments on a previous version of the manuscript.

References

310   Berlich, R. and Harnisch, B.: Radiometric assessment method for diffraction effects in hyperspectral imagers applied to the earth explorer 8
mission candidate flex, in: International Conference on Space Optics — ICSO 2014, edited by Sodnik, Z., Cugny, B., and Karafolas, N.,
vol. 10563, pp. 1475 – 1483, International Society for Optics and Photonics, SPIE, https://doi.org/10.1117/12.2304079, https://doi.org/10.
1117/12.2304079, 2017.

Bovensmann, H., Burrows, J. P., Buchwitz, M., Frerick, J., Noël, S., Rozanov, V. V., Chance, K. V., and Goede, A. P. H.: SCIA-

315   MACHY: Mission Objectives and Measurement Modes, Journal of the Atmospheric Sciences, 56, 127–150, https://doi.org/10.1175/1520-
0469(1999)056<0127:SMOAMM>2.0.CO;2, https://doi.org/10.1175/1520-0469(1999)056<0127:SMOAMM>2.0.CO;2, 1999.

Burrows, J., Hölzle, E., Goede, A., Visser, H., and Fricke, W.: SCIAMACHY—scanning imaging absorption spectrometer for atmospheric
chartography, Acta Astronautica, 35, 445 – 451, https://doi.org/https://doi.org/10.1016/0094-5765(94)00278-T, http://www.sciencedirect.
com/science/article/pii/009457659400278T, earth Observation, 1995.

320   Burrows, J. P., Weber, M., Buchwitz, M., Rozanov, V., Ladstätter-Weißenmayer, A., Richter, A., DeBeek, R., Hoogen, R., Bramstedt, K.,
Eichmann, K.-U., Eisinger, M., and Perner, D.: The Global Ozone Monitoring Experiment (GOME): Mission Concept and First Scientific
Results, Journal of the Atmospheric Sciences, 56, 151–175, https://doi.org/10.1175/1520-0469(1999)056<0151:TGOMEG>2.0.CO;2,
https://doi.org/10.1175/1520-0469(1999)056<0151:TGOMEG>2.0.CO;2, 1999.

Caron, J., Kruizinga, B., and Vink, R.: Slit homogenizers for Earth observation spectrometers: overview on performance, present and future

325   designs, in: International Conference on Space Optics — ICSO 2018, edited by Sodnik, Z., Karafolas, N., and Cugny, B., vol. 11180, pp.
402 – 417, International Society for Optics and Photonics, SPIE, https://doi.org/10.1117/12.2535957, https://doi.org/10.1117/12.2535957,
2019.

Goodman, J. W.: Introduction to Fourier optics, Introduction to Fourier optics, 3rd ed., by JW Goodman. Englewood, CO: Roberts & Co.
Publishers, 2005, 1, 2005.

330   Hu, H., Hasekamp, O., Butz, A., Galli, A., Landgraf, J., Aan de Brugh, J., Borsdorff, T., Scheepmaker, R., and Aben, I.: The operational
methane retrieval algorithm for TROPOMI, Atmospheric Measurement Techniques, 9, 5423–5440, https://doi.org/10.5194/amt-9-5423-
2016, https://amt.copernicus.org/articles/9/5423/2016/, 2016.

Irizar, J., Melf, M., Bartsch, P., Koehler, J., Weiss, S., Greinacher, R., Erdmann, M., Kirschner, V., Albinana, A. P., and Martin, D.: Sentinel-
5/UVNS, in: International Conference on Space Optics — ICSO 2018, edited by Sodnik, Z., Karafolas, N., and Cugny, B., vol. 11180, pp.

335   41 – 58, International Society for Optics and Photonics, SPIE, https://doi.org/10.1117/12.2535923, https://doi.org/10.1117/12.2535923,
2019.

Landgraf, J., aan de Brugh, J., Scheepmaker, R., Borsdorff, T., Hu, H., Houweling, S., Butz, A., Aben, I., and Hasekamp, O.: Carbon
monoxide total column retrievals from TROPOMI shortwave infrared measurements, Atmospheric Measurement Techniques, 9, 4955–
4975, https://doi.org/10.5194/amt-9-4955-2016, https://amt.copernicus.org/articles/9/4955/2016/, 2016.

340   Meister, C., Bauer, M., Keim, C., and Irizar, J.: Sentinel-5/UVNS instrument: the principle ability of a slit homogenizer to reduce scene
contrast for earth observation spectrometer, in: SPIE Proceedings Vol.10423, Sensors, Systems, and Next-Generation Satellites XXI;
104231E, https://doi.org/10.1117/12.2278619, 2017.

Noël, S., Bramstedt, K., Bovensmann, H., Gerilowski, K., Burrows, J. P., Standfuss, C., Dufour, E., and Veihelmann, B.: Quantification
and mitigation of the impact of scene inhomogeneity on Sentinel-4 UVN UV-VIS retrievals, Atmospheric Measurement Techniques, 5,

345   1319–1331, https://doi.org/10.5194/amt-5-1319-2012, https://amt.copernicus.org/articles/5/1319/2012/, 2012.

Sierk, B., Bezy, J.-L., Loescher, A., and Meijer, Y.: The European CO2 Monitoring Mission: observing anthropogenic greenhouse gas emissions from space, in: International Conference on Space Optics — ICSO 2018, edited by Sodnik, Z., Karafolas, N., and Cugny, B., vol. 11180, pp. 237 – 250, International Society for Optics and Photonics, SPIE, https://doi.org/10.1117/12.2535941, https://doi.org/10. 1117/12.2535941, 2019.

350 Thibos, L. N., Applegate, R. A., Schwiegerling, J. T., and and, R. W.: Standards for Reporting the Optical Aberrations of Eyes, in: Vision Science and its Applications, p. SuC1, Optical Society of America, https://doi.org/10.1364/VSIA.2000.SuC1, http://www.osapublishing. org/abstract.cfm?URI=VSIA-2000-SuC1, 2000.

Voors, R., Dobber, M., Dirksen, R., and Levelt, P.: Method of calibration to correct for cloud-induced wavelength shifts in the Aura satellite's Ozone Monitoring Instrument, Appl. Opt., 45, 3652–3658, https://doi.org/10.1364/AO.45.003652, http://ao.osa.org/abstract.cfm?URI=
355 ao-45-15-3652, 2006.